

Nonvolatile Reconfigurable Phase-Change Metadevices for Beam Steering in the Near Infrared

Carlota Ruiz de Galarreta, Arseny M. Alexeev, Yat-Yin Au, Martin Lopez-Garcia, Maciej Klemm, Martin Cryan, Jacopo Bertolotti, and C. David Wright*

The development of flat, compact beam-steering devices with no bulky moving parts is opening up a new route to a variety of exciting applications, such as LIDAR scanning systems for autonomous vehicles, robotics and sensing, free-space, and even surface wave optical signal coupling. In this paper, the design, fabrication and characterization of innovative, nonvolatile, and reconfigurable beam-steering metadevices enabled by a combination of optical metasurfaces and chalcogenide phase-change materials is reported. The metadevices reflect an incident optical beam in a mirror-like fashion when the phase-change layer is in the crystalline state, but reflect anomalously at predesigned angles when the phase-change layer is switched into its amorphous state. Experimental angle-resolved spectrometry measurements verify that fabricated devices perform as designed, with high efficiencies, up to 40%, when operating at 1550 nm. Laser-induced crystallization and reamorphization experiments confirm reversible switching of the device. It is believed that reconfigurable phase-change-based beam-steering and beam-shaping metadevices, such as those reported here, can offer real applications advantages, such as high efficiency, compactness, fast switching times and, due to the nonvolatile nature of chalcogenide phase-change materials, low power consumption.

1. Introduction

During the past decade, metamaterials and metasurfaces have drawn widespread attention due to their potential for manipulating electromagnetic waves spanning from microwave to optical frequencies. Such artificial structures can be engineered on demand to generate effective electromagnetic properties not (or rarely) found in nature,^[1] the most well-known perhaps

being negative refraction.^[1–3] In analogy to the well-established microwave and radio-frequency reflectarrays,^[4,5] optical metasurfaces can also be exploited to mimic the wave front manipulation capabilities of conventional optics, but without the need for bulky optical components,^[6,7] or in the case of beam steering, any moving parts. In such devices, the phase control of light does not rely on propagation effects such as optical path length differences, but instead comes from abrupt local phase shifts introduced by subwavelength resonant elements.^[4–12] Periodic arrays of resonators can therefore be specifically arranged to engineer optical wave fronts essentially at will. Nowadays, a variety of optical and photonic metadevices for wave front shaping, such as flat lenses,^[8,9] hologram generators,^[10] or beam steerers have been reported.^[11–13] However, in most of these approaches, the final configuration is fixed by design,^[2–13] making them unsuitable for applications where light

needs to be controlled dynamically.

Chalcogenide phase-change materials (PCMs), whose refractive index can be selectively controlled, have been used for several years in optical disk storage and more recently for the provision of electrical nonvolatile memories.^[14–18] Lately, the combination of PCMs with metasurfaces has been proposed as a way to create ultrafast, nonvolatile, reconfigurable photonic devices, where the optical response can be tuned and reconfigured on demand.^[19–21] PCMs possess the ability to be switched quickly (nanoseconds or less)^[16] and repeatedly (potentially up to 10^{15} cycles)^[22] between amorphous and crystalline states (or indeed to an intermediate state between the two) by an appropriate thermal, optical, or electrical stimulus.^[14–18] Such atomic rearrangements remain stable at room temperature and come with an abrupt change in the physical properties (e.g., complex refractive index and resistivity).^[15] However, in spite of investigations of the exploitation of this crystalline-to-amorphous electro-optical contrast in PCMs to provide various phase-change metadevices (such as displays, reconfigurable Fresnel zone plates, thermal emitters, absorbers, and filters),^[20,21,23–29] to date no working PCM-enabled beam-steering and beam-shaping metadevices have been experimentally realized. Nevertheless, PCMs have great potential for wave front manipulation,^[30–32] particularly at near-infrared (NIR) and mid-infrared (MIR)

C. R. de Galarreta, Dr. A. M. Alexeev, Dr. Y.-Y. Au,
Dr. J. Bertolotti, Prof. C. D. Wright
College of Engineering
Mathematics and Physical Sciences
University of Exeter
Exeter EX4 4QF, UK
E-mail: david.wright@exeter.ac.uk

Dr. M. Lopez-Garcia,^[†] Dr. M. Klemm, Prof. M. Cryan
Department of Electrical and Electronic Engineering
University of Bristol
Bristol BS8 1TH, UK

 The ORCID identification number(s) for the author(s) of this article can be found under <https://doi.org/10.1002/adfm.201704993>.

^[†]Present address: Nanophotonics Department, International Iberian Nanotechnology Laboratory (INL), 4715-330 Braga, Portugal

DOI: 10.1002/adfm.201704993

wavelengths where they exhibit a high refractive index contrast (between phase states) without significant optical losses.^[33]

In this paper, we design, fabricate, and characterize novel, nonvolatile, reconfigurable beam-steering plasmonic metasurface devices using the prototypical PCM $\text{Ge}_2\text{Sb}_2\text{Te}_5$ (GST), and operating in the NIR spectral range (1530–1570 nm). Our devices can steer beams without any moving parts, reflecting incident light in a mirror-like fashion when the GST layer is crystalline, and anomalously at predefined angles when the GST is amorphous. Our design is based on a simple metal-insulator-metal (MIM) structure, which allows for successful production using common microfabrication techniques. Moreover, in our approach (unlike many others in the literature), the PCM layer is completely protected against oxidation/environmental degradation; its thickness has also been kept to a minimum ($\approx \lambda_0/60$) to facilitate the crystallization and reamorphization processes while minimizing optical losses. Our approach could provide additional advantages with respect to other recently proposed beam-steering technologies (such as those based on free carrier injection^[33]), including fast switching speeds, enhanced efficiency, and, due to the non-volatile nature of PCMs, low power consumption. Steering to multiple angles simultaneously could be achieved by pixelated devices, where each pixel can specifically be designed to steer light at a different angle. PCM-enabled beam-steering metadevices could therefore find application in a range of important fields, such as LIDAR scanning systems for autonomous vehicles, robotics and sensing, imaging, free-space, and even surface wave optical signal coupling.

2. Device Design and Working Principle

The structure of our PCM-based reconfigurable beam-steering device is depicted in **Figure 1a**. It consists of a SiO_2 , ITO, GST, and ITO multilayer stack, sandwiched between a continuous aluminum (Al) bottom plane on Silicon (Si) and a top array of periodically arranged 1D plasmonic Al antennas with different

dimensions (widths). The GST acts essentially as a switchable or tunable dielectric medium that changes the optical behavior of the device. The ITO layers serve a dual role of protecting the GST layer against oxidation from the atmosphere while at the same time providing top and bottom transparent electrodes to allow for electrical or electro-thermal switching of the GST layer.^[11,19] We chose Al for the antennas since, unlike more commonly used plasmonic metals such as Au and Ag, it is CMOS compatible and therefore readily integrated into standard industrial semiconductor fabrication processes, making our design attractive for any future industrial development. A possible disadvantage of using Al for the antenna layer is however its relatively low melting temperature, which is only 40 °C or so above that of GST itself. This means that during amorphization of the GST layer, the Al antennas may melt and distort. However, we did not observe this in our devices (see Section S5 and Figure S8, Supporting Information). In any case, to remove any concerns about possible melting (and subsequent distortion) of the Al antenna layer, it could be encapsulated with a low-loss, low-index dielectric (such as SiO_2) without any appreciable degradation of optical performance.

As shown in **Figure 1b**, when the GST is crystalline, the structure behaves as a mirror-like surface, and thus light is reflected according to conventional specular reflection laws where the angle of reflection θ_r is equal to the angle of incidence θ_i . In the amorphous state, however, the device is specifically designed to operate as an optical metasurface, where each antenna introduces, along the x -axis, linear phase shifts with respect to its neighbor. The sum of these local phase responses results in a constructive interference in a direction different to that of specular reflection (**Figure 1c**). Such a phenomenon is known as anomalous reflection, and the outgoing angle of reflection θ_r in this case is described by the generalized Snell's law^[5,6]

$$\sin \theta_r = \frac{\lambda_0 \Delta\phi}{2\pi d} + \sin \theta_i \quad (1)$$

where λ_0 is the free-space wavelength, $\Delta\phi$ is the phase increment introduced by each antenna element, d is the spacing

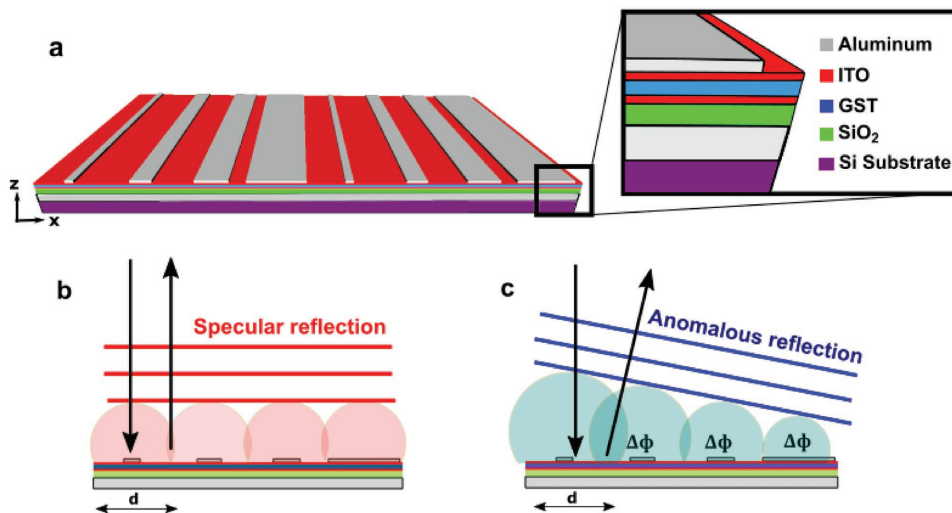


Figure 1. Reconfigurable phase-change beam-steering device design. a) Structure and materials of the device. Huygens principle showing the wave front reconstruction under normal incidence when the GST layer is in the crystalline b), and amorphous c) states.

between elements and θ_i is the angle of incidence. The angle θ_r at which light is reflected anomalously can be engineered (i.e., chosen or designed-in) by changing either $\Delta\phi$ or d , and a maximized phase coverage (ideally of 2π) is desirable in order to increase the number of designs that one can realize.^[5,6]

We choose here a MIM device configuration due to its ability to support antisymmetric states, and thus magnetic plasmon resonances, using dielectric spacers much smaller than the wavelength.^[24,29,34,35] The latter point is especially important, as PCMs need to be melted and rapidly cooled down ($>20\text{ °C ns}^{-1}$) for a successful amorphization process, and this is facilitated by restricting the volume of material that undergoes amorphization.^[14] Optical phase control upon reflection for a particular wavelength is attained by slightly detuning each element from its resonant frequency, which can be achieved by proper design of device geometrical parameters, in particular the antenna width and spacing. Note that here our antenna layer consists of 1D metal strips, a configuration chosen since it simplifies considerably both the device fabrication and simulation processes (cf. 2D patterned antennas). The use of strip antennas means however that our devices are polarization sensitive; essentially, they are designed to work with the polarization direction perpendicular to the strips (TM polarization). Should a polarization-insensitive design be desired, however, this could readily be achieved using antennas comprising a 2D array of squares (see, e.g., ref. [24]).

3. Results and Discussion

3.1. Simulated Device Performance

Our device was designed and optimized for NIR wavelengths, specifically at $\lambda = 1550\text{ nm}$, but note that it could be easily redesigned, using the same device structure, for operation at other desired wavelengths throughout the NIR and MIR spectral range. The scattering properties (i.e., phase and amplitude upon reflection) of the Al plasmonic array were first analyzed via finite element modeling (as described in the Experimental Section), using a generic MIM unit cell depicted in **Figure 2a**. Structures of this form support magnetic plasmon resonances under TM excitation, with such resonances being induced by the coupling of the electric dipole generated in the patch antenna with the bottom aluminum plane. Antisymmetric

states, or curl electric fields, can therefore be induced, which result in a resonant magnetic dipole moment.^[24,34–37] The amplitude and phase response of the unit cell can therefore be tuned by engineering either its geometrical parameters or the complex refractive index of the dielectric spacer (i.e., changing its resonant frequency). Here, the lattice spacing d was fixed to 700 nm to provide a good compromise between reducing unwanted diffraction effects while keeping a sufficiently large spacing between antennas to simplify the fabrication process. The dielectric thickness t was initially fixed to 70 nm , and its absorption coefficient selected to be the same as that of amorphous GST at $\lambda = 1550\text{ nm}$ (i.e., $k = 0.07$), in order to take into account the dielectric losses induced by the PCM. The refractive index n and antenna width A_w were set as variables.

Figure 2b,c shows the simulated results for the amplitude and phase response of the device structure of **Figure 2a**. It can be seen that as the refractive index of the dielectric spacer increases, higher order modes can be excited by increasing the size of A_w in the unit cell. Such resonant behavior can be understood through a simple Fabry–Perot resonator model of the form, $A_w k_0 n_{pp} \approx p\pi - \Delta\phi$, where k_0 is the free-space wave number, n_{pp} is the real part of the effective refractive index of the gap surface plasmon (which depends on the material optical properties and the system geometry), p is an integer defining the order of the mode, and $\Delta\phi$ is the phase delay or phase increment of the reradiated wave.^[36,37] When the refractive index of the dielectric spacer takes values above $n = 3.3$, the higher order modes start to overlap with the fundamental mode, which significantly restricts the phase coverage attainable to below the target value of 2π . Since the refractive index of GST is higher than 3.3 in both amorphous ($n_a = 3.8$) and crystalline ($n_c = 5.6$) states (see Section S1, Supporting Information), it is not possible to fill the dielectric space in the MIM structure of **Figure 2a** entirely with GST and span a suitable phase coverage.^[30] To overcome this fundamental limitation, we therefore here combined a nonlossy low-index dielectric material (SiO_2) layer with a (thin) GST layer to provide the dielectric spacer.

The final device structure is thus as depicted in **Figure 3a**. Here, a 33 nm thick SiO_2 layer fills half of the dielectric spacer volume, and the GST thickness ($t_{\text{gst}} = 26\text{ nm}$) was chosen to be thin enough to prevent overlapping of higher order resonant modes in the amorphous phase, but sufficiently thick to result in a shifting and damping of the resonance after crystallization (which increases both n and k). The GST layer is sandwiched

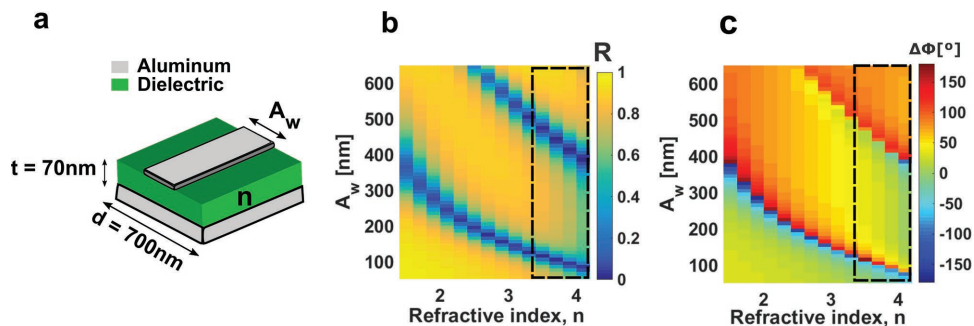


Figure 2. a) Generic MIM plasmonic resonator. Reflectance b) and phase c) as a function of the two variables: refractive index n and Aluminum patch width A_w . The dashed rectangle corresponds to the region where two resonant modes start to overlap (when $n > 3.3$) and thus the target of a near 2π phase control cannot be achieved.

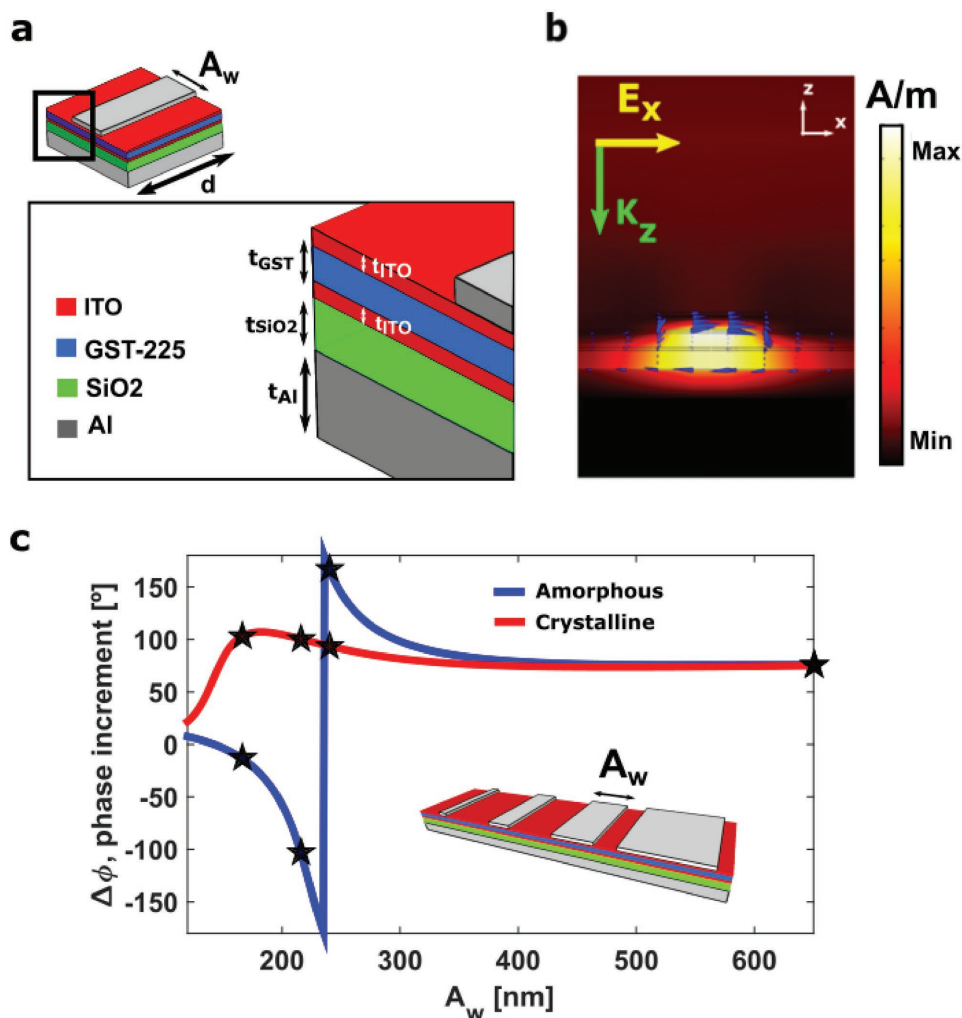


Figure 3. Device structure and design. a) Schematic showing thicknesses and dimensions of the unit cell, where $t_{\text{Al}} = 100$ nm, $t_{\text{SiO}_2} = 33$ nm, $t_{\text{ITO}} = 5$ nm, $t_{\text{GST}} = 26$ nm, and $d = 700$ nm. The width of the top aluminum antenna (A_w) can be varied to tune the optical phase response upon reflection. b) Numerically resolved instantaneous magnetic field distribution when the unit cell is in resonance. The blue cones represent the current loops responsible of the magnetic dipole resonance. c) Phase increment of reradiated wave as a function of A_w for both amorphous (blue) and crystalline (red) states of the GST layer. The stars correspond to the antenna sizes selected to build the supercell represented by the inset ($A_{w1} = 166$ nm, $A_{w2} = 214$ nm, $A_{w3} = 239$ nm, and $A_{w4} = 650$ nm).

between two 5 nm thick ITO films to, as previously described, protect the GST from oxidation and to provide top and bottom electrodes for in situ electrical or electro-thermal switching approaches.^[11,19]

The presence of a plasmon magnetic resonance in the designed structure is confirmed by the results of Figure 3b, where a strong enhancement of the magnetic field (surrounded by currents flowing in opposite directions) between the Al patch and the bottom Al plane can clearly be identified (here for the case of a patch Al antenna width of $A_w = 222$ nm). To obtain the required phase coverage, the antenna width was varied from 100 to 650 nm, and the resulting phase shift upon reflection was calculated. Results are shown in Figure 3c and reveal a total phase coverage of $\approx 300^\circ$ when the GST layer is in the amorphous phase. After GST crystallization, however, the resonant frequency of each element is shifted due to an increase of the refractive index n , and the response is damped (i.e., the Q

factor is reduced) as a consequence of an increase in the absorption coefficient k . This results in a near invariant optical phase response for all antenna widths shown, so leading to specular mirror-like reflection (see Section S2, Supporting Information for further details). Both crystalline and amorphous states together span a phase range of 360° , which suggests that the unit cell could be used to create a wide range of different beam-steering configurations, by combining amorphous and crystalline antennas. For this specific device, however, we chose four “amorphous antennas” with each imposing a phase increment along the x -axis of $\Delta\phi = 90^\circ$ and yielding the super-cell arrangement shown in the inset of Figure 3c. According to Equation (1), for a period of $d = 700$ nm and a wavelength $\lambda = 1550$ nm, such arrangement gives an anomalous angle of reflection $\theta_r = 33.6^\circ$ when the GST layer is amorphous. After crystallization, the linear phase gradient along the surface is cancelled, leading to ordinary reflection with $\theta_i = \theta_r$ (in fact there is not, as might be

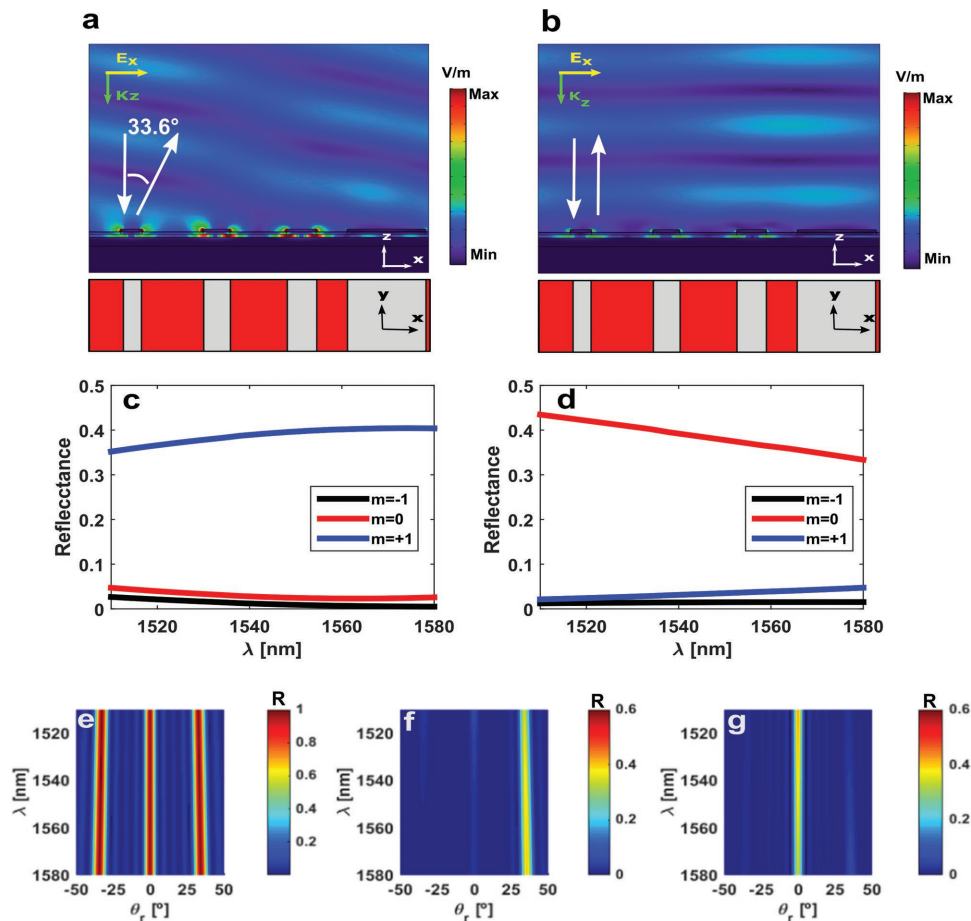


Figure 4. Instantaneous electric field distribution under normal incidence excitation, confirming: a) anomalous reflection ($\theta_r = 33.6^\circ$) when the GST layer is amorphous, b) ordinary specular reflection when the GST layer is crystalline. Numerically resolved reflectance of the three diffraction orders ($m = -1$, $m = 0$, and $m = +1$) when the device is amorphous c), and crystalline d). e) Normalized far-field radiation pattern for an array of supercells. Angular and spectral response of the device for its two operational modes: anomalous reflection when the GST layer is amorphous f), and specular reflection in the crystalline state g).

expected, perfect cancellation, but the maximum phase difference between the first and last antennas of the supercell is here only around 17° when the GST layer in the crystalline state).

The predicted final performance of our PCM-enabled metadvice was assessed via simulation of an infinite array of the supercells shown in Figure 3c (the inset). Figure 4a,b shows the instantaneous electric field distributions under normal incidence conditions confirming anomalous reflection when the GST layer is amorphous, and ordinary mirror-like reflection when crystallized. The spectral and angular characteristics of the device were then analyzed via grating and antenna theory. The far-field behavior can be interpreted in a similar way to a conventional diffraction grating of period $\Lambda = 2800$ nm,^[35,39] but with the majority of the reradiated power concentrated in the first diffraction order ($m = +1$) when the GST is amorphous, and in the zeroth order ($m = 0$) when it is crystalline. Figure 4c shows the numerically computed reflectance of the three diffraction orders ($m = \pm 1$, $m = 0$), over a range of wavelengths from 1515 to 1580 nm. The anomalous reflectance ($m = +1$) is, over this range, always above 36% while the residual ordinary reflectance ($m = 0$) is less than 4%. With the GST

layer crystalline, ordinary reflection dominates ($m = 0$), with an overall reflection efficiency above 32% and a small residual anomalous reflection ($m = +1$) below 5%. The best compromise between amorphous and crystalline states is located at the design wavelength ($\lambda = 1550$ nm) with 40% reflection efficiency for each operational mode (note that the missing energy is absorbed by the array as plasmonic and dielectric losses in the aluminum and ITO/GST, respectively).

The far-field radiation pattern of the device of Figure 4c was calculated independently via the array factor (AF), which under normal incidence conditions becomes^[4]

$$AF^2 = \frac{1}{N^2} \left[\frac{\sin\left(\frac{Nk_0 \Lambda \sin(\theta_r)}{2}\right)}{\sin\left(\frac{k_0 \Lambda \sin(\theta_r)}{2}\right)} \right]^2 \quad (2)$$

Here, Λ is the period of the supercell (here made of 4 elements and with $\Lambda = 2800$ nm), θ_r is the radial coordinate in reflection, and N is the number of supercells taken into account (which has direct influence on the width of the diffraction lobes).

Figure 4e shows the normalized far-field distribution calculated using Equation (2) for $N = 10$.

The final radiation pattern containing both spectral and angular characteristics of the device was then calculated by multiplying the numerically obtained reflectance coefficients of the three diffraction orders shown in Figure 4c,d by the radiation pattern calculated via Equation (2). Figure 4f,g shows the results for the amorphous and crystalline states of the GST layer, i.e., for anomalous and ordinary specular reflection, respectively.

3.2. Device Characterization

Our PCM-enabled beam-steering metadevices were fabricated, as described in the Experimental Section, to the above design. Figure 5a,b shows, respectively, optical and scanning electron microscopy (SEM) images of typical as-fabricated

structures (note that in total around 150 devices were made). Devices were characterized using an angle-resolved NIR Fourier imaging micro-spectrometer, as described in Section S4 in the Supporting Information. Figure 5c,d shows the results from these measurements, compared with simulations for both amorphous and crystalline states of the GST, respectively. The experimental angular reflectance was calculated by normalizing raw measurements to the maximum power reflected from a silver mirror. It can be seen in Figure 5c that indeed the as-fabricated device reflects anomalously with the GST layer in the amorphous phase. The anomalous reflection angle is $\theta_r \approx 33 \pm 3^\circ$, matching, within experimental error, the design angle of 33.6° . The overall efficiency across the whole spectral band (from 1515 to 1580 nm) when operating in anomalous reflection mode was found to be above 34%, again in line with design predictions (numerical simulation). After thermal crystallization, the device reflects in an ordinary specular fashion at $\theta_r = 0^\circ$, with an efficiency across the range of wavelengths

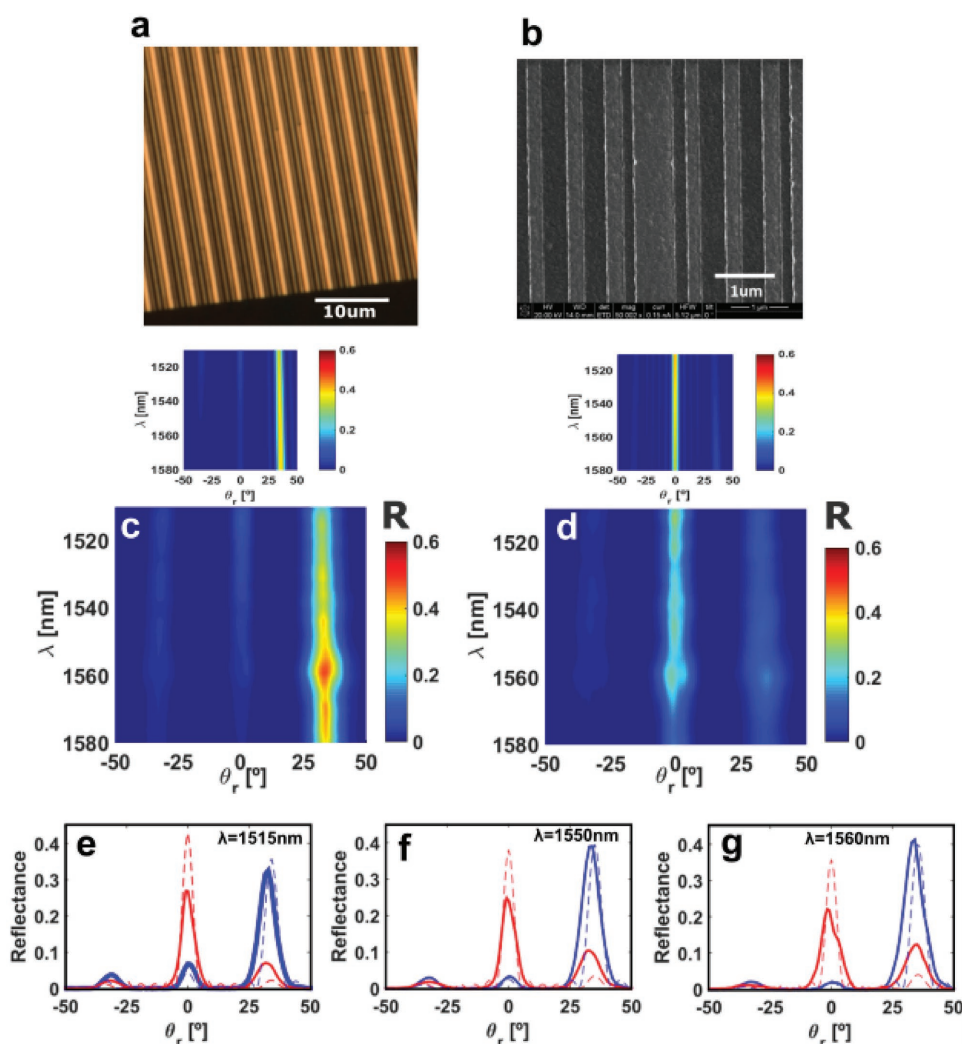


Figure 5. PCM-enabled metadvice characterization. a) Optical microscope image of a typical as-fabricated structure, where the aluminum plasmonic resonators can be identified. b) SEM image of the device showing fine details across two supercells. Measured angular reflectance compared with simulations across the spectral region of interest for both amorphous c) and crystalline d) GST states. Transverse 2D plots showing details of the measured angular reflectance (solid) against numerical simulations (dashed) at three different wavelengths: e) $\lambda = 1515$ nm, f) $\lambda = 1550$ nm, and g) $\lambda = 1560$ nm.

measured above 22% (cf. 32% from the numerical simulations). This small discrepancy could be caused by a mismatch (between simulations and experiment) of the complex refractive index of crystalline GST, as well as device fabrication errors (e.g., on the thicknesses and antenna sizes). Previous studies of Al plasmonic resonators (for other applications) show that a native oxide layer forming around the Al resonators (not taken into account in our simulations) might also contribute to the small deviations between the designed and actual responses of our devices.^[27,40]

In Figure 5e–g, we show the measured angular reflectance (solid curve) of the as-fabricated devices, compared with simulations (dashed curve) for both anomalous (blue) and specular (red) reflections and at $\lambda = 1515, 1550,$ and 1560 nm, respectively. At the design wavelength ($\lambda = 1550$ nm), the agreement between experiment and simulation for the GST in the amorphous state is striking, with only a small decrease in device performance (cf. simulation) for the crystalline state. The best balance between states was found at 1515 nm with $\approx 30\%$ of light being reflected both anomalously (at $\approx 32^\circ$ at this wavelength) and specularly (i.e., at 0°).

Finally, the reversibility of our metadevices, i.e., their ability to be switched between amorphous and crystalline states over repeated cycles, was demonstrated via optically induced heating using a scanned 405 nm laser. Laser scans were first performed on unpatterned device structures (i.e., structures without the top Al antenna array) to determine the laser parameters (in terms of power, pulse duration, and repetition rate) required for effective switching (see Section S4, Supporting Information for specific details). **Figure 6a** shows four images of an unpatterned device area after two successive crystallization and reamorphization cycles (or SET/RESET cycles in PCM terminology), where a change in reflectance on changing phase is clearly apparent (crystal regions are relatively lighter than amorphous regions, since the crystal state has a higher reflectance in the visible part of the spectrum). To provide more quantitative evidence of successful switching, NIR reflectance spectra (over the range 1000 – 1600 nm) were also measured after each crystallization (SET) and reamorphization (RESET) process, and the results compared with spectra obtained from devices in the as-deposited amorphous state and from devices that had been fully crystallized by a thermal annealing process (hot plate annealing

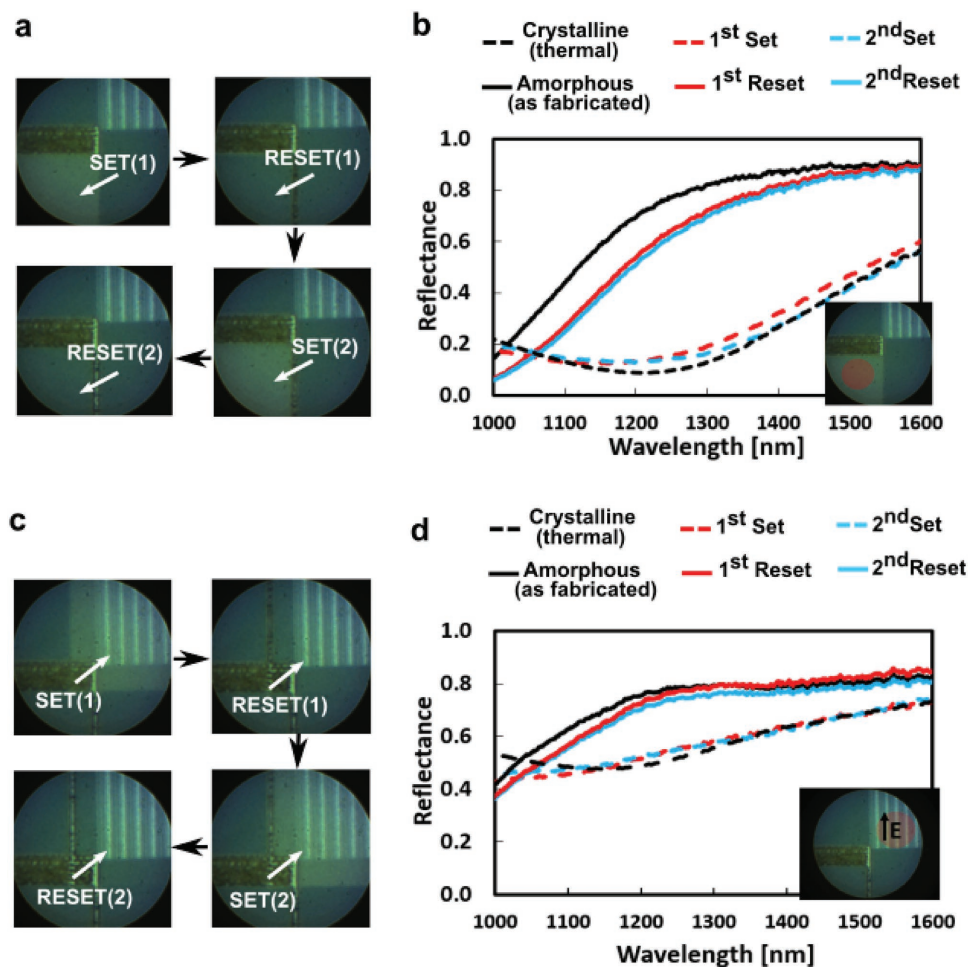


Figure 6. a) Optically induced phase-change experiments carried out in an unpatterned region of the device. A change in color can be appreciated after each SET/RESET. b) Experimental reflectance spectra of the unpatterned region after each cycle, compared with fully amorphous (as fabricated) and fully crystalline (thermally crystallized) spectra. c) Optically induced phase-change experiments carried out inside the device. d) Experimental reflectance spectra of the device under TE polarization, again compared with fully amorphous and fully crystalline states.

at 200 °C for 10 min). Figure 6b shows the results from these measurements and reveal very good agreement between the NIR spectra for as-deposited amorphous/thermally crystallized samples and those subjected to the optically induced phase changes, which confirms that successful switching between states had occurred in the unpatterned device region. The above experiment was then repeated for completed devices (i.e., in regions with the top-patterned Al antenna array). The resulting microscope images are shown in Figure 6c and the corresponding NIR reflectance spectra in Figure 6d (for TE illumination, which is more effective than the TM mode at revealing the phase change using reflectance measurements, see Section S5, Supporting Information). Again, very good agreement between the NIR spectra for optically switched devices and the fully amorphous (as-deposited) and fully crystalline (thermally induced) cases confirms successful laser-induced switching of the device itself. For real-time in situ device switching, the ultimate goal, the bottom metal plane (suitably patterned) could be used as a resistive heater (such thermally induced switching of GST layers has been successfully demonstrated)^[41] or alternatively the ITO layers could be used as top and bottom electrodes in an electrical switching arrangement (again, such an approach that has been demonstrated successfully before in both experiment and simulation).^[20,24]

4. Conclusions

We have successfully demonstrated how to combine PCMs with plasmonic metasurfaces to create novel, nonvolatile, reconfigurable beam-steering and beam-shaping metadevices working in the NIR. The relative simplicity of our design, based as it is on a MIM resonator type structure, has led to successful device realization using common microfabrication techniques. Experimental angle-resolved spectral Fourier microscopy, along with detailed numerical simulations, has confirmed that as-fabricated devices reflect an incident optical beam in a specular mirror-like fashion when the phase-change layer is in the crystalline state, but reflect anomalously at predesigned angles when the phase-change layer is switched into its amorphous state. In addition, dynamic switching between states was successfully achieved using optical excitations from an ex situ laser. Moreover, our device design is inherently suited to possible in situ switching between states using thermal (resistive heating) or, due to the incorporation of ITO layers into the device structure, electrical means. The use of ITO capping layers also ensures that the phase-change layer in our device is protected from atmospheric oxidation, an important but often overlooked consideration. Our metadvice can easily be configured to steer light at different angles by changing the arrangement and/or spacing between individual antenna elements, and to steer at multiple angles by using a pixelated arrangement (with different pixels steering at different angles). Bidirectional and polarization-independent steering could also be implemented by substituting the 1D strip-like antennas by polarization-independent 2D squares.^[24,34] In addition, our approach can deliver a full 2π phase coverage by combining amorphous and crystalline antennas, which suggests that our basic design could be used to create other types of reconfigurable photonic devices,

such as dynamic hologram generators. The same basic structure could be redesigned for other NIR and MIR spectral bands, where GST exhibits low losses and high refractive index contrast.^[33] The nonvolatile nature of PCMs, along with their inherently high switching speeds, also promises devices with low power consumption and fast operation. We thus anticipate that phase-change-enabled metadevices, such as we have demonstrated here, will find use in technologically important beam-steering and beam-shaping applications.

5. Experimental Section

Numerical Simulations: Both design and analysis stages of the device were performed using finite element methods enabled by the commercial software package COMSOL Multiphysics (RF module). Values for the refractive index n and absorption coefficient k for the various materials used in the device were taken from the literature, except those for GST, which were acquired experimentally through reflectance measurements (see Section S1, Supporting Information for details). All the models described in this paper were meshed using triangular elements with a maximum size of $\lambda_0/(50n)$ in dielectric and semiconductor materials, and of $\lambda_0/100$ in aluminum. The wave equation was solved via plane wave excitation under normal incidence, with Floquet periodic boundary conditions applied to the sides to mimic infinite arrays of elements.

Device Fabrication: The PCM-enabled beam-steering metadevices (having an overall area of $70 \times 70 \mu\text{m}^2$) were fabricated as follows. First, the (bottom) Al, SiO₂, (bottom) ITO, GST, and (top) ITO layers were deposited onto a clean silicon substrate using magnetron sputtering in an Ar atmosphere (base pressure 2.0×10^{-4} Pa, Ar pressure 1.3×10^{-2} Pa). DC sputtering was used for the deposition of conductive materials, RF sputtering for the SiO₂. Next, aluminum plasmonic resonators were created on top of the layered structure by using e-beam lithography to create an appropriate resist mask into which the top Al layer was sputter deposited, followed by a standard lift-off process. More specifically, a 250 nm layer of positive e-beam PMMA resist (950K A4) was spin coated (6000 rpm) onto the sample and baked at low temperatures (70 °C) for 15 min to harden the resist but avoiding crystallization of the GST layer (the as-deposited GST state was amorphous). The e-beam lithography was carried out using a NanoBeam nB4 (Nanobeam Ltd.) system to write the Al antennas patterns (80 kV, 1.5 nA, exposure doses ranging between 4 and 11 C m⁻² in increments of 0.25 C m⁻²; optimum doses were found to lie between 7 and 8 C m⁻²). The resist was developed in 15:5:1 IPA to MIBK to EMK solution for 30 s. Finally, aluminum was sputtered inside the pattern, using the same conditions as for the bottom aluminum layer. The PMMA/aluminum mask was then removed by first delaminating most of the film using warm acetone flow from a pipette and subsequent soft sonication in acetone for 5 min. Morphological analysis of the samples was carried out using optical microscopy and SEM. An explanatory figure showing the fabrication steps can be found in Section S3 in the Supporting Information.

Experimental Characterization: Both spectral and angular characteristics of the devices were measured in a circular area of 20 μm radius using IR angle-resolved Fourier-imaging micro-spectroscopy, with a SuperK COMPACT supercontinuum laser as a white light source, and a NIR spectrometer (Ocean Optics NIRQUEST-512). This technique had previously been successfully used to measure the scattering properties of photonic crystals and dielectric metasurfaces.^[35,38] See Section S4 in the Supporting Information for detailed information and schematics of the experimental setup.

Crystallization (SET) and reamorphization (RESET) cycling experiments were carried out, on both “blanket” film structures and as-fabricated devices in areas of $40 \times 40 \mu\text{m}$, by a scanning-pulsed laser (405 nm) focused into an $\approx 0.5 \mu\text{m}$ diameter spot through an Olympus LMPLFLN50x objective (NA 0.5). Each scan took several minutes, and verification of the occurrence of phase switching as a result of such

experiments was achieved by measuring the reflectance in situ using a BWTEK sol 1.7 NIR spectrometer, and comparing with results from thermally crystallized devices. Further details of the laser parameters and experimental procedures used can be found in Section S5 in the Supporting Information.

Supporting Information

Supporting Information is available from the Wiley Online Library or from the author.

Acknowledgements

C.D.W. acknowledges funding via the US Naval Research Laboratories ONRC programme (#N62909-16-1-2174) and the EPSRC ChAMP and WAFT grants (EP/M015130/1 and EP/M015173/1). C.R.d.G. acknowledges funding via the EPSRC CDT in Metamaterials (EP/L015331/1). M.L.G. acknowledges funding via the EPSRC grant EP/M009033/1.

Conflict of Interest

The authors declare no conflict of interest.

Keywords

beam steering, phase-change materials, phased arrays, photonic metadevices, plasmonic metasurfaces, reflectarrays

Received: August 30, 2017

Revised: October 23, 2017

Published online:

- [1] L. Solymar, E. Shamonina, *Waves in Metamaterials*, Oxford University Press, Oxford **2009**.
- [2] R. A. Shelby, D. R. Smith, S. C. Nemat-Nasser, S. Schultz, *Appl. Phys. Lett.* **2001**, *78*, 489.
- [3] H. J. Lezec, J. A. Dionne, H. A. Atwater, *Science* **2007**, *316*, 430.
- [4] J. Huang, J. A. Encinar, *Reflectarray Antennas*, Wiley-IEEE Press, New Jersey, USA **2007**.
- [5] J. A. Zornoza, R. L. eberer, J. A. Encinar, W. Menzel, *IEEE Trans. Antennas Propag.* **2006**, *54*, 210.
- [6] N. Yu, F. Capasso, *Nat. Mater.* **2014**, *13*, 139.
- [7] N. Yu, P. Genevet, F. Aieta, M. A. Kats, R. Blanchard, G. Aoust, J.-P. Tetienne, *IEEE J. Sel. Top. Quantum Electron.* **2013**, *19*, 4700423.
- [8] F. Aieta, P. Genevet, M. A. Kats, N. Yu, R. Blanchard, Z. Gaburro, F. Capasso, *Nano Lett.* **2012**, *12*, 4932.
- [9] F. Aieta, P. Genevet, M. Kats, F. Capasso, *Opt. Express* **2013**, *21*, 31530.
- [10] B. Walther, C. Helgert, C. Rocksuhl, F. Setzpfandt, F. Eilenberg, E.-B. Kley, F. Lederer, A. Tunnermann, T. Pertsch, *Adv. Mater.* **2012**, *24*, 6300.
- [11] L. Zou, W. Withayachumnankul, C. M. Shah, A. Mitchell, M. Bhaskaran, S. Sriram, C. Fumeaux, *Opt. Express* **2013**, *21*, 1344.
- [12] T. Niu, W. Withayachumnankul, B. S. Y. Ung, H. Menekse, M. Bhaskaran, S. Sriram, C. Fumeaux, *Opt. Express* **2013**, *21*, 2875.
- [13] J. Ginn, B. Lail, J. Alda, G. Boreman, *Opt. Lett.* **2008**, *33*, 779.
- [14] M. Wuttig, N. Yamada, *Nat. Mater.* **2007**, *6*, 824.
- [15] Y. Ohta, *J. Optoelectron. Adv. Mater.* **2001**, *3*, 609.
- [16] D. Loke, T. H. Lee, W. J. Want, L. P. Shi, R. Zao, Y. C. Yeo, T. C. Chong, S. R. Elliott, *Science* **2012**, *336*, 1566.
- [17] W. J. Wang, D. Loke, L. T. Law, L. P. Shi, R. Zhao, M. H. Li, L. Chen, H. X. Tang, Y. C. Yeo, A. O. Adeyeye, T. C. Chong, A. L. Lacaita, in *Int. Electron Devices Meet.*, 2012, IEEE, San Francisco, CA, USA **2012**, p. 31.3.1.
- [18] M. Wuttig, *Nat. Mater.* **2005**, *4*, 265.
- [19] J. P. Turpin, J. A. Bossard, K. L. Morgan, D. H. Werner, P. L. Werner, *Int. J. Antennas Propag.* **2014**, *2014*, 29837.
- [20] P. Hosseini, C. D. Wright, H. Bhaskaran, *Nature* **2014**, *511*, 206.
- [21] Q. Wang, E. T. F. Rogers, B. Gholipour, C.-M. Wang, G. Yuan, J. Teng, N. I. Zheludev, *Nat. Photonics* **2016**, *10*, 60.
- [22] I. S. Kim, S. L. Cho, D. H. Im, E. H. Cho, D. H. Kim, G. H. Oh, D. H. Ahn, S. O. Park, S. W. Nam, J. T. Moon, C. H. Chung, in *2010 IEEE Symp. VLSI Technol.* IEEE, Honolulu, HI, USA **2010**, pp. 203.
- [23] K. K. Du, Q. Li, T.-B. Lyu, J.-C. Ding, Y. Lu, Z.-Y. Cheng, M. Qiu, *Light: Sci. Appl.* **2017**, *6*, e16194.
- [24] S. Garcia-Cuevas Carrillo, G. R. Nash, H. Hayat, M. J. Cryan, M. Klemm, H. Bhaskaran, C. D. Wright, *Opt. Express* **2016**, *24*, 12563.
- [25] B. Gholipour, J. Zhang, K. F. MacDonald, D. W. Hewak, N. I. Zheludev, *Adv. Mater.* **2013**, *25*, 2050.
- [26] A.-K. U. Michel, D. N. Chifrin, T. W. W. Mab, K. Schonauer, M. Salinga, M. Wutting, T. Taubner, *Nano Letters* **2013**, *13*, 2470.
- [27] W. Dong, Y. Qiu, J. Yang, R. E. Simpson, T. Cao, *J. Phys. Chem. C* **2016**, *120*, 12713.
- [28] T. Cao, R. E. Simpson, M. J. Cryan, *J. Opt. Soc. Am. B* **2013**, *30*, 439.
- [29] Y. Qu, Q. Li, K. Du, L. Cai, J. Lu, M. Qiu, *Laser Photonics Rev.* **2017**, *11*, 1700091.
- [30] L. Zou, M. Cryan, M. Klemm, *Opt. Express* **2014**, *22*, 24142.
- [31] C. H. Chu, M. L. Tseng, J. Chen, P. C. Wu, Y.-H. Chen, H.-C. Wang, T.-Y. Chen, W. T. Hsieh, H. J. Wu, G. Sun, D. P. Tsai, *Laser Photonics Rev.* **2016**, *10*, 986.
- [32] T. Cao, G. Zheng, S. Wang, C. Wei, *Opt. Express* **2015**, *23*, 18029.
- [33] K. Shportko, S. Kremers, M. Woda, D. Lencer, J. Robertson, M. Wuttig, *Nat. Mater.* **2008**, *7*, 653.
- [34] Y.-W. Huang, H. W. H. Lee, R. Sokhoyan, R. A. Pala, K. Thyagarajan, S. Han, D. P. Tsay, H. A. Atwater, *Nano Lett.* **2016**, *16*, 5319.
- [35] L. Zou, M. Lopez-Garcia, W. Withayachumnankul, C. M. Shah, A. Mitchell, M. Bhaskaran, S. Sriram, R. Oulton, M. Klemm, C. Fumeaux, *Appl. Phys. Lett.* **2014**, *105*, 191109.
- [36] A. Pors, S. I. Bozhevolnyi, *Opt. Express* **2013**, *21*, 27438.
- [37] T. Sondergaard, J. Jung, S. I. Bozhevolnyi, G. D. Valle, *New J. Phys.* **2008**, *10*, 105008.
- [38] L. Chen, M. Lopez-Garcia, M. P. C. Taverne, X. Zheng, Y.-L. D. Ho, J. G. Rarity, *Opt. Letters* **2017**, *42*, 1584.
- [39] S. Larouche, D. R. Smith, *Opt. Lett.* **2012**, *37*, 2391.
- [40] C. Langhammer, M. Schwind, B. Kasemo, I. Zoric, *Nano Lett.* **2008**, *8*, 1461.
- [41] Y.-Y. Au, H. Bhaskaran, C. D. Wright, *Sci. Rep.* **2017**, *7*, 9688.